THE JOURNAL OF PHYSICAL CHEMISTRY Letters

Letter

Cite This: J. Phys. Chem. Lett. 2019, 10, 6857−6864

pubs.acs.org/JPCL

Understanding the Improvement in the Stability of a Self-Assembled Multiple-Quantum Well Perovskite Light-Emitting Diode

Cheng Li,*[,†,‡] Nana Wang,[§] Antonio Guerrero,[∥] Yu Zhong,[‡] Huan Long,[‡] Yanfeng Miao,[§] Juan Bisquert,[∥] Jianpu Wang,*[,§] and Sven Huettner*[,‡]

[†]School of Electronic Science and Engineering, Xiamen University, Xiamen 361005, China

[‡]Department of Chemistry, University of Bayreuth, Universitätstrasse 30, 95447 Bayreuth, Germany

[§]Key Laboratory of Flexible Electronics (KLOFE) and Institute of Advanced Materials (IAM), Jiangsu National Synergetic Innovation Center for Advanced Materials (SICAM), Nanjing Tech University (NanjingTech), 30 South Puzhu Road, Nanjing 211816, China

[∥]Institute of Advanced Materials (INAM), Universitat Jaume I, 12006 Castello, Spain

Supporting Information

ABSTRACT: We fabricate two-dimensional Ruddlesden−Popper layered perovskite films by introducing 1-naphthylmethylamine iodide into the precursor, which forms a self-assembled multiple-quantum well (MQW) structure. Enabling outstanding electroluminescence properties, light-emitting diodes (LEDs) using the MQW structure also demonstrate significant improvement in stability in comparison with the stability of devices made from formamidinium lead iodide. To understand this, we perform electroabsorption spectroscopy, wide-field photoluminescence imaging microscopy and impedance spectroscopy. Our approach enables us to determine the mobility of iodide ions in MQW perovskites to be $(1.5 \pm 0.8) \times 10^{-8}$ cm^2 V^{-1} s^{-1}, ∼2 orders of magnitude lower than that in three-dimensional perovskites. We highlight that activated ion migration is a requirement for a degradation pathway in which a steady supply of ions is needed to modify the perovskite/external contact interfaces. Therefore, the improvement in stability in a MQW perovskite LED is directly attributed to the suppressed ion migration due to the inserted organic layer acting as a barrier for ionic movement.

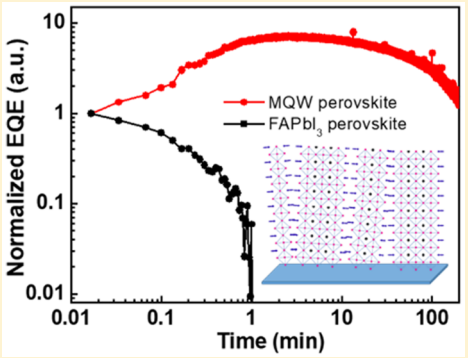

Light-emitting diodes (LEDs) based on organometal halide perovskites (PeLED) are undergoing a rapid development, and their external quantum efficiencies (EQEs) have recently been shown to exceed 20%.[1−4] Despite these remarkable achievements, the quest for more stable and higher-efficiency devices continuously motivates the investigation of members of the perovskite family. Two-dimensional (2D) Ruddlesden−Popper (RP) layered perovskites emerge as very suitable candidates for optoelectronic devices in terms of ambient stability.[5,6] Nevertheless, in pure 2D RP perovskites, the cost of improved stability is the sacrifice of charge transport due to the insulating nature of the large organic cations between lead halide octahedral (PbX_6) layers.[7] To establish a trade-off between device performance and stability, it is intriguing to utilize quasi-2D perovskites, or multilayered 2D perovskites, i.e., a mixture of different numbers of PbX_6 layers with different band gaps.[8,9] Among them, a multiple-quantum well (MQW) perovskite with cascade energy levels has attracted more attention in LEDs showing remarkably high EQEs and stabilities.[10,11] This outstanding performance of MQW PeLEDs is attributed to effective charge confinement in small regions and negligible photoluminescence (PL) quenching at the interfacial area between different band gap regions.[12−15]

Unlike photovoltaic devices, which work at a maximum power point (approaching the flat-band condition), LEDs operate continuously under high external driving voltage and/or current. The lifetime of perovskite solar cells has increased to thousands of hours.[16,17] However, typical lifetimes of three-dimensional (3D) PeLEDs are less than a few hours,[18,19] although they can be significantly improved by passivating surface defects.[1,20] Evidence reveals that the defects and/or ions in perovskites play an essential role in device performance, e.g., hysteresis,[21,22] stability,[8,16] and light emission.[23] However, a systematic investigation of ion dynamics in these low-dimensional layered perovskites,[24−26] especially in MQW structures, is still insufficient. Additionally, the role of ion migration in device stability is still not fully elucidated.[17,27,28] In this work, we present a correlation of ion migration and device performance/stability in self-assembled MQW PeLEDs.

Received: August 22, 2019
Accepted: September 27, 2019
Published: September 27, 2019

DOI: 10.1021/acs.jpclett.9b02467
J. Phys. Chem. Lett. 2019, 10, 6857−6864

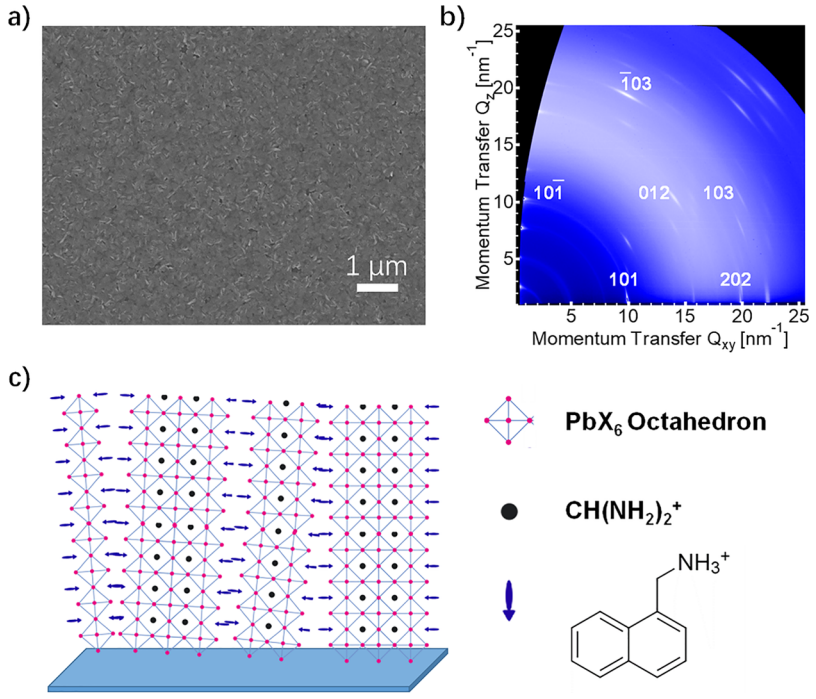

Figure 1. (a) Scanning electron microscopy image of a MQW film on a glass substrate. (b) GIWAXS pattern of a MQW perovskite film on a glass substrate. (c) Schematic diagram for the MQW perovskite structure and preferentially vertical alignment on a substrate, based on the calculation of Figure S1.

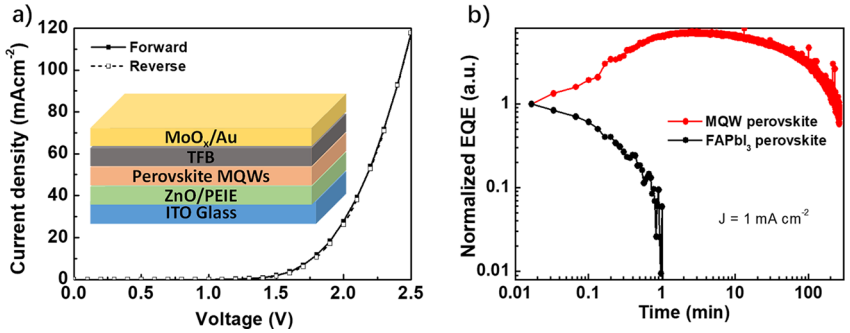

Figure 2. (a) Current density−voltage (J−V) curve of a MQW PeLED. The inset is the schematic diagram of a MQW PeLED structure. The scanning speed is 0.05 V/s. (b) Test of the stability of both MQW and $FAPbI_3$ PeLEDs under a constant current density of 1 mA/cm^2.

In this work, we fabricate RP layered perovskite films by introducing 1-naphthylmethylamine iodide (NMAI) into the precursor, which forms a self-assembled MQW structure. Figure 1a shows a scanning electron microscopy (SEM) image of a typical MQW film processed on a glass substrate with a flat and dense surface morphology. The X-ray diffraction (XRD) pattern (Figure S1) of the MQW perovskite film reveals that a distribution of n values exists, i.e., the layer thickness of the 2D sections.[29−31] To characterize the perovskite crystalline orientation, grazing-incidence wide-angle X-ray scattering (GIWAXS) measurements were performed. As shown in Figure 1b, alongside the continuous diffraction rings on the extended arc segment, which indicates the existence of random crystal orientation, there are also clear sporadic Bragg spots within the rings. This implies the existence of single-crystal diffraction and/or ordered alignment of the crystal.[32] The detailed orientation analysis, i.e., Herman's orientation factor calculation, is included in Figure S1. In combination with the ultraviolet visible (UV−vis) absorption spectra (Figure S2), we can identify the existence of a MQW structure, forming quantum wells of different sizes inside the film, ranging from n = 1, 2, and 3 to larger values. The prevalence of different quantum well sizes leads to a cascaded energy transfer among the QWs, which is visible in a sharp low-energy emission.[10,19] It is noted that the sharp distinct Bragg spot at (101) suggests an improved preferred orientation along the out-of-plane direction, as shown in the schematic diagram (Figure 1c).[18] In a vertically configured device, e.g., inset of Figure 2a, this orientation can facilitate suitable charge transport along the out-of-plane direction.[31,33,34]

The inset of Figure 2a shows the schematic configuration of a MQW PeLED. Figure 2a presents the forward and backward J−V curve of the device. A figure on a log scale and consecutive scans are shown in Figure S3a. Compared with other 3D PeLEDs, e.g., $CH_3NH_3PbI_{3-x}Cl_x$,[35] the hysteresis of the MQW perovskite devices is significantly suppressed. We note that, in MQW PeLEDs, as shown in Figure 2b, the device lifetime improves by ∼2 orders of magnitude under a constant current density of 1 mA/cm^2 compared to that of conventional $FAPbI_3$ PeLEDs. In addition, MQW PeLEDs exhibit a significantly

DOI: 10.1021/acs.jpclett.9b02467
J. Phys. Chem. Lett. 2019, 10, 6857−6864

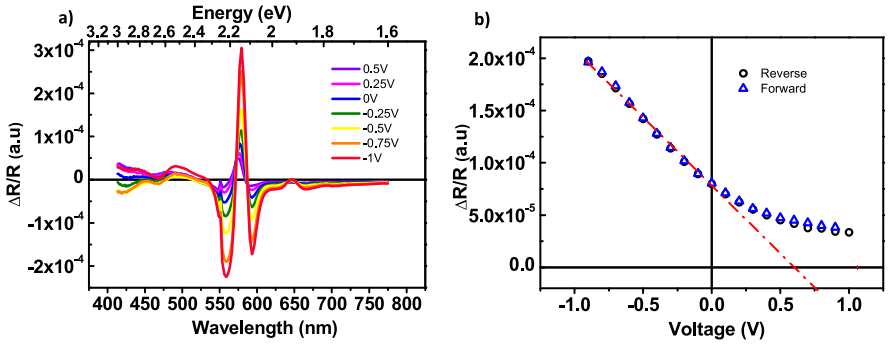

Figure 3. (a) EA spectra of a TiO_2/MQW perovskite/Au device for a series of dc voltages. (b) Voltage dependence of the EA amplitude at a photon energy of 2.15 eV.

enhanced stability under high driving voltages (see a comparison in Figure S3). For example, the radiance intensity at $\gtrsim$2 V of a $FAPbI_3$ PeLED is no longer stable, whereas the intensity of a MQW PeLED still increases with driving voltages up to 3.7 V (Figure S3b). This significant improvement makes MQW perovskites promising candidates for next-generation optoelectronic devices.

First, to explore the stability of the crystalline structure of a MQW perovskite, we carried out the *in situ* GIWAXS measurement under an external electric field, based on a laterally configured electrode structure (Figure S4c). By applying 200 V on the interdigitated electrode device with a channel length of 200 μm at room temperature, we find the comparison of the initial and final GIWAXS patterns (after 13 min) indicates negligible crystal structure decomposition, as exhibited in Figure S4. In contrast to other perovskite films, e.g., $CH_3NH_3PbI_{3-x}Cl_x$ as reported previously,[36] this result also demonstrates significantly improved stability under an external electric field.

Electroabsorption (EA) spectroscopy has been demonstrated to be a powerful approach for studying the excitonic properties,[37,38] Rashba splitting,[39] lattice expansion,[17] and electric dipole moment[40] of perovskite materials. In this work, we employed EA spectroscopy as a non-invasive tool to investigate the built-in potential of MQW perovskite devices.[41]

As described in detail previously,[42,43] with the aid of a lock-in amplifier technique, EA spectroscopy can measure field-modulated light absorption spectra. In a film with a uniform internal field, the EA response at the fundamental frequency of the applied ac bias, $\left.\frac{\Delta R}{R}\right|_{\omega}$, can be expressed as[44]

$$\left.\frac{\Delta R}{R}\right|_{\omega} \propto \mathrm{Im}\,\chi^{(3)}(h\nu)(V_{dc} - V_{BI})V_{ac}\sin(\omega t) \quad (1)$$

where $\mathrm{Im}\chi^{(3)}(h\nu)$ is the imaginary part of the third order of the electric susceptibility, V_{dc} and V_{ac} are the applied external dc and ac voltages, respectively, V_0 is the internal dc voltage, and V_{BI} is the built-in potential in the device. A comparison between an EA spectrum and an UV−vis absorption spectrum is shown in Figure S5. It shows that the EA spectrum corresponds to a second derivative of the absorption spectrum, which implies the existence of permanent dipoles.[40,41] Figure 3a shows the EA spectra of a TiO_2/MQW perovskite/Au device under a series of dc voltages. The shapes of these spectra reveal the independence of the external dc voltage, indicating that it is the Stark effect that plays the dominant role in these spectra.[44] When the photon energy is fixed at 2.15 eV, a photon energy with the highest signal-to-noise ratio, voltage-dependent EA amplitudes are obtained (see Figure 3b). First, it is found that the nulling voltage is around 0.7 V, reflecting the work function difference between TiO_2 and Au, which gives rise to V_{BI}.[43] Second, as expected, in contrast to a 3D $CH_3NH_3PbI_{3-x}Cl_x$ perovskite device (as shown in Figure S6b), there is no significant built-in potential shift during the sweeping of dc voltages, which is consistent with the absence of $J-V$ hysteresis in Figure 2a. It is accepted that the formation of a charge injection barrier, due to the interplay between charges and accumulated mobile ions at the perovskite/electrode interface, plays an essential role in an occurring $J-V$ hysteresis.[21] This absence of a potential shift suggests the lack of the existence of charge accumulation at the opposite electrode/perovskite interfaces, yet it is important to mention that when sweeping towards higher voltages, the shift in built-in potential occurs again (illustrated in Figure S7). This implies that ion migration is still prevalent, probably due to the existence of high-n domains within the perovskite composition. This result clearly points to a reduced supply of ions to the external interfaces due to a reduced level of ion migration in the bulk of the MQW perovskite, and stabilization of the double layer occurs only at lower frequencies.

To further study the accumulation of ions at the external interfaces, we studied the capacitance−voltage response using techniques previously described for perovskite devices based on $CH_3NH_3PbI_{3-x}Cl_x$.[36] In particular, we observe that capacitive techniques are useful for understanding ionic migration toward the external electrodes as the capacitance in the low-frequency region is related to ion migration and a double-layer polarization of the electrode.[28] Capacitance−frequency results are shown in Figure 4a for devices measured under no applied dc bias (0 V) and a modulated ac voltage perturbation. These results for the $CH_3NH_3PbI_{3-x}Cl_x$ perovskite are very similar to those of our previous studies of charge accumulation. In particular, the capacitance values of 3.7 F cm^{-2} measured at low frequencies (20 mHz) are similar to those previously reported (1.9 F cm^{-2}). Interestingly, the measured MQW perovskite shows the onset of ion migration at frequencies of 0.1 Hz, ~3 orders of magnitude lower than in the 3D $CH_3NH_3PbI_{3-x}Cl_x$ perovskite (100 Hz). This result clearly indicates that ion migration is not kinetically favored in the case of the MQW perovskites, which requires longer times to effectively observe the double-layer capacitance arising from ion migration. As one can see in Figure 4b for a given applied dc bias, the capacitance due to the double layer is always lower for the MQW perovskites. As shown in the previous works, the thermalized distribution of ions can be approximated by the formula

DOI: 10.1021/acs.jpclett.9b02467
J. Phys. Chem. Lett. 2019, 10, 6857−6864

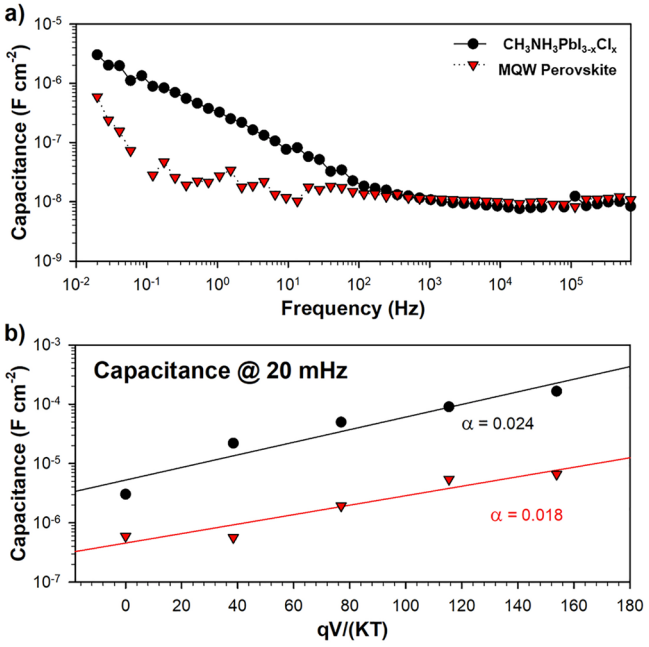

Figure 4. (a) Capacitance−frequency measurements of a 3D $CH_3NH_3PbI_{3-x}Cl_x$ and a MQW perovskite film at an applied dc bias of 0 V with ac voltage perturbation with different frequencies. (b) Capacitance measured at 20 mHz measured as a function of the applied dc bias. The device structure is shown in Figure S4c.

$$C = C_0 e^{\alpha qV/k_B T} \quad (2)$$

where $C_0 = C_1$, which is the capacitance at zero bias,[36] and a parameter α of $^1/_2$ corresponds to the thermalized accumulation of freely diffusing ions according to their electrochemical potential. q, k_B, T, and V are the charge, Boltzmann constant, absolute temperature, and external voltage, respectively. However, the experimental observations reported in Figure 4b show that an α of $^1/_2$ is far from being satisfied. Results for an α of ∼0.025 of the $CH_3NH_3PbI_{3-x}Cl_x$ perovskite are very similar to those previously reported and slightly higher than for the MQW perovskite ($\alpha \sim 0.018$). The increase in capacitance does not correspond simply to the thermalized distribution of ions, but to an exponential distribution of states characterized by a temperature parameter T_0 as $\alpha = T/T_0$.[45]

The ionic migration/transport/conduction within traditional perovskite oxide materials (ABO_3)[46] and solid-state electrolytes[47,48] has been intensively studied in past several decades. Temperature-dependent stepwise-stabilized current responses, or chronoamperometry, have been used to obtain the involved activation energy.[41,49] As shown in Figure 5a, the current increases after each voltage step can be fitted by a biexponential function. It is found that two distinct processes exist in the time-dependent current behavior, a fast one on a time scale of ∼1 s and a much slower one on a time scale of ∼10 s. Further study of the temperature-dependent behavior of these spectra indicates that (1) the fast dynamic behavior is nearly independent of temperature and might be due to the electronic conduction[24,50] and (2) the slower one shows a temperature dependence as indicated in Figure 5b. By fitting of an Arrhenius relation,[49] $\Gamma = \Gamma_0 \exp\left(\frac{-E_a}{k_B T}\right)$ is obtained. Γ is the rate of the thermally activated process obtained from the current decay/rise behavior, which is due to an ionic equilibration process. T is the absolute temperature, and k_B is the Boltzmann constant. This temperature-dependent measurement reveals an activation energy E_a of 0.48 ± 0.09 eV, via measurement of four different devices for better averaging. On the basis of previous studies of $CH_3NH_3PbI_{3-x}Cl_x$ and $FAPbI_3$ perovskites, it is found that the activation energy of iodide ions/vacancies is mostly within the range of 0.1−0.3 eV.[21] Hence, this increased activation energy suggests a larger barrier for the ionic migration in these MQW perovskite films. This enhanced barrier is attributed to the inserted hydrophobic organic cations, which suppresses ion migration.[24] Note that there is still a gap in the activation energy between a single crystal, ∼1 eV,[51] and this MQW perovskite film. This gap suggests the prospect of further improving the quality of the film and optimizing the structure as well as 3D−2D composition. Furthermore, considering the perpendicular orientation of the MQW perovskites with respect to the substrate and the fact that a vertical device geometry has been used (shown in Figure 1c), it seems that the MQW structure also reduces the level of ionic migration in parallel with the MQWs. This nicely implies that the long organic molecules within quasi-2D materials also passivate grain boundaries in polycrystalline films, impeding ionic or vacancy migration.[52]

To characterize the ion migration in these materials *in situ*, we use an *in situ* wide-field PL imaging technique while applying a bias. This method has been demonstrated previously[16,36] and offers the possibility of investigating both the spatial and the temporal evolution of PL inactive areas under an external electric field simultaneously.[28] Figure 6 shows both the spatial and the temporal evolution of PL inactive areas under a voltage of 100 V across an ∼200 μm

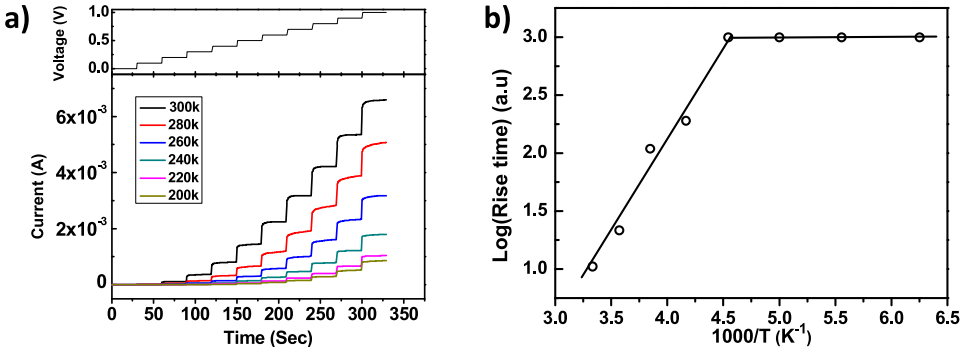

Figure 5. (a) Temperature-dependent current vs time when applying voltages ranging from 0 to 1 V under dark vacuum conditions. The device architecture is TiO_2/MQW perovskite/Au. (b) Rise time vs 1000/T at a fixed external voltage of 0.5 V. The slope is calculated as 3800 K.

DOI: 10.1021/acs.jpclett.9b02467
J. Phys. Chem. Lett. 2019, 10, 6857−6864

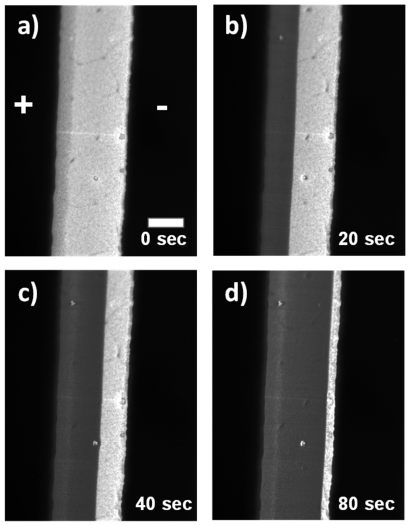

Figure 6. (a–d) Ion migration characterization under an external electrical field (~0.5 V/μm) using wide-field PL imaging microscopy at different time intervals. The scale bar is 100 μm. The excitation intensity is ~35 mW/cm with a wavelength of 440 nm, and the exposure time per image is 200 ms. A video is provided in the Supporting Information.

channel length, and the device configuration is depicted in Figure S4c. At 0 s, in Figure 6a, the bright area represents the high-PL emission of a pristine MQW perovskite film. Upon application of an external dc electrical field, around 0.5 V/μm, a sharp front of PL inactive area appears at the positive electrode and moves toward the negative one. A complete video is included in the Supporting Information. These PL inactive areas are attributed to electric field-driven halide ions/vacancies.[50,53,54] In brief, due to the low-temperature fabrication, defect states exist, such as iodide- and lead-related defects/ions, for example, Frenkel defects. This initial doping level can be changed by the moving species, for instance, iodide vacancies under an external electric field. As a consequence, these moving vacancies can modulate (1) the local doping level, which results in a change in the conductivity of the film, and (2) the local charge recombination ratio, which strongly influences the PL intensity. The latter is due to the prevalence of interstitial defects, which remained as the more mobile vacancies migrated away. Those interstitials act as nonradiative recombination centers. Therefore, by monitoring the moving front of the PL quenching area and the time-dependent current, we are able to quantitatively characterize the ionic mobility.

To quantitatively characterize the ion movement, according to our recent iodide vacancy migration model,[28,50] we determined that the ionic mobility (μ) is $(1.5 \pm 0.8) \times 10^{-8}$ $cm^2\ V^{-1}\ s^{-1}$ by fitting the time-dependent current curve in four different individual devices. The detailed calculation is presented in Figure S9. Compared with those of $CH_3NH_3PbI_3$ perovskites,[50] this ionic mobility decreases by approximately 1–2 orders of magnitude, consistent with the enhanced activation energy. Here, we must mention that the observation of Figure 4a, which is the onset of the capacitive process at the perovskite/electrode interface, shows that it has become slower by 2 orders of magnitude at low frequencies. The consistency of the activation energy and wide-field PL imaging characterization including a capacitive process suggests that the interface/surface and bulk ionic migration process are correlated.

In conclusion, we found that a MQW PeLED demonstrates strongly improved stability compared to that of $FAPbI_3$ LED perovskites, increasing by ~2 orders of magnitude in duty time and enhanced stability performance, especially at higher driving voltages. By incorporating a group of characterization techniques, we have quantitatively investigated ion migration in MQW perovskite materials: there is no interfacial modulation demonstrated by electroabsorption studies, the activation energy of ions is significantly increased, and the ionic movement is significantly impeded as shown by *in situ* PL imaging studies under an external bias. This goes hand in hand with a significantly reduced level of interfacial ion accumulation as detected by impedance spectroscopy. We attribute these improvements to the suppressed ion migration toward the contacts where interface modification leads to chemical reactions and degradation. In addition, both lateral and vertical device structures have been used in these studies, whereby the MQWs show a strong orientation perpendicular to the substrates. Interestingly, the decreased ionic/vacancy migration is viable in both directions of the MQWs. These characteristics enable the MQW perovskite to serve as a prospective candidate for the next-generation LED materials. For the next step of the materials design and optimization process, the crystalline orientation and optimal 3D–2D composition and structure will be some of the most important topics for device stability and performance.

EXPERIMENTAL METHODS

Perovskite MQW Film Fabrication. Formamidinium iodide (FAI) was purchased from Tokyo Chemical Industry Co. (TCI), all the other chemicals were purchased from Sigma-Aldrich and used as received.

1-Naphthylmethylamine iodide (NMAI) was synthesized by adding 4.34 g of hydroiodic acid (45 wt % in water) to a stirring solution of 1-naphthalenemethylamine (12.72 mmol) in tetrahydrofuran (THF, 50 mL) at 0 °C for 2 h. Then, the solution was evaporated at 50 °C to obtain the NMAI precipitate. This product was washed three times with a THF/CH_2Cl_2 (3:1) mixture and then dried under vacuum. MQW perovskite precursor solutions were prepared by dissolving NMAI, FAI, and PbI_2 with a molar ratio of 2:1:2 in *N*,*N*-dimethylformamide (DMF) (10 wt %) in a nitrogen-filled glovebox.

Glass substrates were washed with acetone and isopropanol for 10 min individually. Then, these glass substrates were treated within ozone for ~10 min at 50 °C. In a nitrogen-filled glovebox, the precursor solution was spin-coated on the glass substrates at 3000 rpm for 60 s. Then, the as-spun films were annealed at 100 °C for ~15 min in the glovebox. These samples were transferred into an evaporation chamber with a pressure of $\sim 3 \times 10^{-6}$ mbar, and an ~70 nm thickness of Au was deposited by thermal evaporation through an interdigitating shadow mask. This geometry of the mask was as follows. Electrode distance L was 200 μm, and a ratio between channel width W and length L was 500. After that, a 40 mg/mL poly(methyl methacrylate) (PMMA) solution dissolved in butyl acetate (anhydrous, 99%) was spin-coated on the film at a speed of 2000 rpm for 60 s in the glovebox. In the end, by using an Ultrasonic Soldering System (USS-9200, MBR electronics GmbH), external conducting wires were connected to the electrodes.

DOI: 10.1021/acs.jpclett.9b02467
J. Phys. Chem. Lett. 2019, 10, 6857–6864

For EA measurements, samples were prepared as previously described. Fluorine-doped tin oxide ($F:SnO_2$) (FTO)-coated glass was patterned with Zn powder and a HCl solution. FTO glasses were washed successively with acetone, 2% hellmanex diluted in deionized water, deionized water, and isopropanol for 10 min each. A compact TiO_2 layer was deposited by spraying a solution of titanium diisopropoxide bis-(acetylacetonate) (0.6 mL) in ethanol (21.4 mL) at 450 °C for 90 min under an ambient atmosphere. As in previous devices, after the precursor had been spin-coated, the samples were annealed and deposited with a Au electrode. In the end, a 40 mg/mL PMMA solution dissolved in butyl acetate was spin-coated on the film at a speed of 2000 rpm for 60 s as a protection layer.

In Situ GIWAXS Experiment. GIWAXS measurements were performed at the SAXS/WAXS beamline at the Australian Synchrotron. During the experiment, 12 keV photons were used, equipped with 2D scattering patterns recorded on a Dectris Pilatus 1M detector. The distance between the sample and detector was calibrated with a silver behenate sample.

Fabrication and Characterization of LEDs. The device has an ITO/polyethylenimine ethoxylated (PEIE)-modified zinc oxide (ZnO, ∼20 nm)/perovskite (∼30 nm)/poly[9,9-dioctyl-fluorene-*co*-*N*-(4-butylphenyl)diphenylamine] (TFB, ∼40 nm)/molybdenum oxide (MoO_x, ∼7 nm)/gold (Au, ∼60 nm) structure. The ITO substrates were washed with acetone and isopropanol for 10 min and then treated with oxygen plasma for 10 min. Colloidal ZnO nanocrystals were spin-coated at 4000 rpm for 45 s and annealed at 150 °C for 30 min. Then, an ultrathin PEIE layer was deposited on ZnO layers. The 3D (3:1 FAI:PbI_2 molar ratio) and MQW (2:1:2 NMAI:FAI:PbI_2 molar ratio) perovskites were spin-coated onto the PEIE-modified ZnO films at 4000 rpm for 45 s and annealed at 100 °C for 10 min. TFB dissolved in *m*-xylene was spin-coated on the perovskite films at 2000 rpm for 45 s. Finally, the MoO_x/Au anodes were evaporated through a mask. The device area was 0.03 cm^{-2} as defined by the overlapping area of ITO and Au. The devices were measured by a combination of a Keithley 2400 source meter and a fiber integration sphere (FOIS-1) coupled with a QE65 Pro spectrometer in a nitrogen-filled glovebox.

Impedance Spectroscopy. The dc voltage source for polarizing the sample was a potentiostat equipped with a frequency analyzer (Autolab PGSTAT-30). A small ac perturbation was applied, and the differential current output was measured to calculate the impedance response. The frequency window was kept small, ranging between 10 kHz and 100 mHz, to minimize the measurement time.

Electroabsorption Spectroscopy. The light source was installed within a monochromator illuminator (Oriel Company). The light going through a monochromator (SPEX 1681B, Horiba Scientific) illuminated the device and was reflected back from the Au electrode onto a photodiode (HUV-4000B, EG&G Judson). A dual-channel lock-in amplifier (SR 830, Stanford Research Systems) was used to bias the device with a dc and an ac voltage and monitored the ac amplitude of the EA signal from the photodiode. The ac voltage was set to 1 V at a frequency of 2013 Hz. In the meantime, the dc amplitude of the EA signal was recorded with a digital multimeter (HP34401A, Hewlett-Packard Co.).

PL Imaging Microscopy. This experiment was based on a modified commercial PL microscopy experiment (Microscope Axio Imager.A2m, Zeiss). The sample was arranged in the focal plane of an objective lens (10×/0.25 HD, Zeiss). The sample was illuminated by an internal LED illuminator using a filter (HC 440 SP, AHF analysentechnik AG), which provides the excited light at a wavelength of ∼440 nm. The excitation light intensity was set to ∼35 mW/cm^2. The PL signal was filtered (HC-BS 484, AHF analysentechnik AG) to remove the residual excited light and then directed onto a high-speed CCD camera (Pco. Pixelfly, PCO AG). The exposure time was set to 200 ms. An external dc voltage of 100 V was applied between the Au electrodes using a Sourcemeter (236 Source Measure Unit, Keithley Co.), and the time-dependent current was recorded by a LabVIEW program.

■ ASSOCIATED CONTENT

Supporting Information

The Supporting Information is available free of charge on the ACS Publications website at DOI: 10.1021/acs.jpclett.9b02467.

Details of SEM, X-ray diffraction, GIWAXS, Herman's orientation analysis, UV−vis absorption, and photoluminescence spectra, comparison of the performance of $FAPbI_3$ and MQW perovskite LEDs, GIWAXS pattern under an external electric field, electroabsorption spectrum, dc voltage-dependent EA spectra, PL inactive front moving speed as a function of the external electric field, and the electrical current as a function of time of a MQW film (PDF)

Video for the ion migration process recorded by PL imaging microscopy (AVI)

■ AUTHOR INFORMATION

Corresponding Authors

*E-mail: chengli@xmu.edu.cn.
*E-mail: iamjpwang@njtech.edu.cn.
*E-mail: sven.huettner@uni-bayreuth.de.

ORCID

Cheng Li: 0000-0003-0282-7899
Antonio Guerrero: 0000-0001-8602-1248
Yu Zhong: 0000-0002-2313-8227
Juan Bisquert: 0000-0003-4987-4887
Jianpu Wang: 0000-0002-2158-8689
Sven Huettner: 0000-0002-2566-1898

Notes

The authors declare no competing financial interest.

■ ACKNOWLEDGMENTS

The authors gratefully acknowledge the financial support by the Joint Research Program between China and European Union (2016YFE0112000), the Major Research Plan of the National Natural Science Foundation of China (91733302), the Bavarian State Ministry of Science, Research, and the Arts for the Collaborative Research Network "Solar Technologies go Hybrid" and Federal Ministry of Education. The authors also thank financial support by the German Academic Exchange service (DAAD) through its Thematic Network Melbourne-Bayreuth Polymer/Colloid Network and the German Research Foundation (DFG). Part of this research was carried out at the Australian Synchrotron at the SAXS/WAXS beamline. A.G. and J.B. acknowledge funding from MINECO of Spain (MAT2016-76892-C3-1-R and RYC-2014-16809) and University Jaume I (UJI-B2017-32). C.L. acknowledges

DOI: 10.1021/acs.jpclett.9b02467
J. Phys. Chem. Lett. 2019, 10, 6857−6864

funding from the National Natural Science Foundation of China (61974126 and 51902273). N.W., Y.M., and J.W. acknowledge funding from the Natural Science Foundation of Jiangsu Province, China (BK20180085), the National Natural Science Foundation of China (61875084), the National Science Fund for Distinguished Young Scholars (61725502).

REFERENCES

(1) Cao, Y.; Wang, N.; Tian, H.; Guo, J.; Wei, Y.; Chen, H.; Miao, Y.; Zou, W.; Pan, K.; He, Y.; et al. Perovskite light-emitting diodes based on spontaneously formed submicrometre-scale structures. *Nature* **2018**, *562*, 249−253.

(2) Lin, K.; Xing, J.; Quan, L. N.; de Arquer, F. P. G.; Gong, X.; Lu, J.; Xie, L.; Zhao, W.; Zhang, D.; Yan, C.; et al. Perovskite light-emitting diodes with external quantum efficiency exceeding 20%. *Nature* **2018**, *562*, 245−248.

(3) Zhao, B.; Bai, S.; Kim, V.; Lamboll, R.; Shivanna, R.; Auras, F.; Richter, J. M.; Yang, L.; Dai, L.; Alsari, M.; et al. High-efficiency perovskite−polymer bulk heterostructure light-emitting diodes. *Nat. Photonics* **2018**, *12*, 783−789.

(4) Chiba, T.; Hayashi, Y.; Ebe, H.; Hoshi, K.; Sato, J.; Sato, S.; Pu, Y.-J.; Ohisa, S.; Kido, J. Anion-exchange red perovskite quantum dots with ammonium iodine salts for highly efficient light-emitting devices. *Nat. Photonics* **2018**, *12*, 681−687.

(5) Saidaminov, M. I.; Mohammed, O. F.; Bakr, O. M. Low-dimensional-networked metal halide perovskites: The next big thing. *ACS Energy Lett.* **2017**, *2*, 889−896.

(6) Qi, X.; Zhang, Y.; Ou, Q.; Ha, S. T.; Qiu, C.-W.; Zhang, H.; Cheng, Y.-B.; Xiong, Q.; Bao, Q. Photonics and optoelectronics of 2D metal-halide perovskites. *Small* **2018**, *14*, 1800682.

(7) Quan, L. N.; Yuan, M.; Comin, R.; Voznyy, O.; Beauregard, E. M.; Hoogland, S.; Buin, A.; Kirmani, A. R.; Zhao, K.; Amassian, A.; et al. Ligand-stabilized reduced-dimensionality perovskites. *J. Am. Chem. Soc.* **2016**, *138*, 2649−2655.

(8) Wang, Z.; Lin, Q.; Chmiel, F. P.; Sakai, N.; Herz, L. M.; Snaith, H. J. Efficient ambient-air-stable solar cells with 2D−3D hetero-structured butylammonium-caesium-formamidinium lead halide perovskites. *Nat. Energy* **2017**, *2*, 17135.

(9) Bai, Y.; Xiao, S.; Hu, C.; Zhang, T.; Meng, X.; Lin, H.; Yang, Y.; Yang, S. Dimensional engineering of a graded 3D−2D halide perovskite interface enables ultrahigh Voc enhanced stability in the p-i-n photovoltaics. *Adv. Energy. Mater.* **2017**, *7*, 1701038.

(10) Wang, N.; Cheng, L.; Ge, R.; Zhang, S.; Miao, Y.; Zou, W.; Yi, C.; Sun, Y.; Cao, Y.; Yang, R.; et al. Perovskite light-emitting diodes based on solution-processed self-organized multiple quantum wells. *Nat. Photonics* **2016**, *10*, 699.

(11) Yuan, M.; Quan, L. N.; Comin, R.; Walters, G.; Sabatini, R.; Voznyy, O.; Hoogland, S.; Zhao, Y.; Beauregard, E. M.; Kanjanaboos, P.; et al. Perovskite energy funnels for efficient light-emitting diodes. *Nat. Nanotechnol.* **2016**, *11*, 872.

(12) Chang, J.; Zhang, S.; Wang, N.; Sun, Y.; Wei, Y.; Li, R.; Yi, C.; Wang, J.; Huang, W. Enhanced performance of red perovskite light-emitting diodes through the dimensional tailoring of perovskite multiple quantum wells. *J. Phys. Chem. Lett.* **2018**, *9*, 881−886.

(13) Zhang, S.; Yi, C.; Wang, N.; Sun, Y.; Zou, W.; Wei, Y.; Cao, Y.; Miao, Y.; Li, R.; Yin, Y.; et al. Efficient red perovskite light-emitting diodes based on solution-processed multiple quantum wells. *Adv. Mater.* **2017**, *29*, 1606600.

(14) Li, M.; Gao, Q.; Liu, P.; Liao, Q.; Zhang, H.; Yao, J.; Hu, W.; Wu, Y.; Fu, H. Amplified spontaneous emission based on 2D Ruddlesden−Popper perovskites. *Adv. Funct. Mater.* **2018**, *28*, 1707006.

(15) Yantara, N.; Bruno, A.; Iqbal, A.; Jamaludin, N. F.; Soci, C.; Mhaisalkar, S.; Mathews, N. Designing efficient energy funneling kinetics in Ruddlesden−Popper perovskites for high-performance light-emitting diodes. *Adv. Mater.* **2018**, *30*, 1800818.

(16) Bai, S.; Da, P.; Li, C.; Wang, Z.; Yuan, Z.; Fu, F.; Kawecki, M.; Liu, X.; Sakai, N.; Wang, J. T.-W.; et al. Planar perovskite solar cells with long-term stability using ionic liquid additives. *Nature* **2019**, *571*, 245−250.

(17) Tsai, H.; Asadpour, R.; Blancon, J.-C.; Stoumpos, C. C.; Durand, O.; Strzalka, J. W.; Chen, B.; Verduzco, R.; Ajayan, P. M.; Tretiak, S.; et al. Light-induced lattice expansion leads to high-efficiency perovskite solar cells. *Science* **2018**, *360*, 67−70.

(18) Tsai, H.; Nie, W.; Blancon, J.-C.; Stoumpos, C. C.; Soe, C. M. M.; Yoo, J.; Crochet, J.; Tretiak, S.; Even, J.; Sadhanala, A.; et al. Stable light-emitting diodes using phase-pure Ruddlesden−Popper layered perovskites. *Adv. Mater.* **2018**, *30*, 1704217.

(19) Yang, M.; Wang, N.; Zhang, S.; Zou, W.; He, Y.; Wei, Y.; Xu, M.; Wang, J.; Huang, W. Reduced Efficiency Roll-Off and Enhanced Stability in Perovskite Light-Emitting Diodes with Multiple Quantum Wells. *J. Phys. Chem. Lett.* **2018**, *9*, 2038−2042.

(20) Miao, Y.; Ke, Y.; Wang, N.; Zou, W.; Xu, M.; Cao, Y.; Sun, Y.; Yang, R.; Wang, Y.; Tong, Y.; et al. Stable and bright formamidinium-based perovskite light-emitting diodes with high energy conversion efficiency. *Nat. Commun.* **2019**, *10*, 3624.

(21) Li, C.; Guerrero, A.; Zhong, Y.; Huettner, S. Origins and mechanisms of hysteresis in organometal halide perovskites. *J. Phys.: Condens. Matter* **2017**, *29*, 193001.

(22) Yuan, Y.; Huang, J. Ion migration in organometal trihalide perovskite and its impact on photovoltaic efficiency and stability. *Acc. Chem. Res.* **2016**, *49*, 286−293.

(23) Booker, E. P.; Thomas, T. H.; Quarti, C.; Stanton, M. R.; Dashwood, C. D.; Gillett, A. J.; Richter, J. M.; Pearson, A. J.; Davis, N. J. L. K.; Sirringhaus, H.; et al. Formation of long-lived color centers for broadband visible light emission in low-dimensional layered perovskites. *J. Am. Chem. Soc.* **2017**, *139*, 18632−18639.

(24) Lin, Y.; Bai, Y.; Fang, Y.; Wang, Q.; Deng, Y.; Huang, J. Suppressed ion migration in low-dimensional perovskites. *ACS Energy Lett.* **2017**, *2*, 1571−1572.

(25) Xiao, X.; Dai, J.; Fang, Y.; Zhao, J.; Zheng, X.; Tang, S.; Rudd, P. N.; Zeng, X. C.; Huang, J. Suppressed ion migration along the in-plane direction in layered perovskites. *ACS Energy Lett.* **2018**, *3*, 684−688.

(26) Huang, Z.; Proppe, A. H.; Tan, H.; Saidaminov, M. I.; Tan, F.; Mei, A.; Tan, C.-S.; Wei, M.; Hou, Y.; Han, H.; et al. Suppressed ion migration in reduced-dimensional perovskites improves operating stability. *ACS Energy Lett.* **2019**, *4*, 1521−1527.

(27) Kim, G. Y.; Senocrate, A.; Yang, T.-Y.; Gregori, G.; Grätzel, M.; Maier, J. Large tunable photoeffect on ion conduction in halide perovskites and implications for photodecomposition. *Nat. Mater.* **2018**, *17*, 445−449.

(28) Kim, S.-G.; Li, C.; Guerrero, A.; Yang, J.-M.; Zhong, Y.; Bisquert, J.; Huettner, S.; Park, N.-G. Potassium ions as a kinetic controller in ionic double layers for hysteresis-free perovskite solar cells. *J. Mater. Chem. A* **2019**, *7*, 18807.

(29) Zhang, T.; Long, M.; Yan, K.; Qin, M.; Lu, X.; Zeng, X.; Cheng, C. M.; Wong, K. S.; Liu, P.; Xie, W.; et al. Crystallinity preservation and ion migration suppression through dual ion exchange strategy for stable mixed perovskite solar cells. *Adv. Energy Mater.* **2017**, *7*, 1700118.

(30) Milot, R. L.; Sutton, R. J.; Eperon, G. E.; Haghighirad, A. A.; Martinez Hardigree, J.; Miranda, L.; Snaith, H. J.; Johnston, M. B.; Herz, L. M. Charge-carrier dynamics in 2D hybrid metal−halide perovskites. *Nano Lett.* **2016**, *16*, 7001−7007.

(31) Zhang, X.; Wu, G.; Fu, W.; Qin, M.; Yang, W.; Yan, J.; Zhang, Z.; Lu, X.; Chen, H. Orientation regulation of phenylethylammonium cation based 2D perovskite solar cell with efficiency higher than 11%. *Adv. Energy Mater.* **2018**, *8*, 1702498.

(32) Qing, J.; Liu, X.-K.; Li, M.; Liu, F.; Yuan, Z.; Tiukalova, E.; Yan, Z.; Duchamp, M.; Chen, S.; Wang, Y.; et al. Aligned and graded type-II Ruddlesden−Popper perovskite films for efficient solar cells. *Adv. Mater.* **2018**, *8*, 1800185.

(33) Tsai, H.; Nie, W.; Blancon, J.-C.; Stoumpos, C. C.; Asadpour, R.; Harutyunyan, B.; Neukirch, A. J.; Verduzco, R.; Crochet, J. J.; Tretiak, S.; et al. High-efficiency two-dimensional Ruddlesden−Popper perovskite solar cells. *Nature* **2016**, *536*, 312.

DOI: 10.1021/acs.jpclett.9b02467
J. Phys. Chem. Lett. 2019, 10, 6857−6864

(34) Yang, R.; Li, R.; Cao, Y.; Wei, Y.; Miao, Y.; Tan, W. L.; Jiao, X.; Chen, H.; Zhang, L.; Chen, Q.; et al. Oriented quasi-2D perovskites for high performance optoelectronic devices. *Adv. Mater.* **2018**, *30*, 1804771.
(35) Tan, Z.-K.; Moghaddam, R. S.; Lai, M. L.; Docampo, P.; Higler, R.; Deschler, F.; Price, M.; Sadhanala, A.; Pazos, L. M.; Credgington, D.; et al. Bright light-emitting diodes based on organometal halide perovskite. *Nat. Nanotechnol.* **2014**, *9*, 687.
(36) Li, C.; Guerrero, A.; Zhong, Y.; Gräser, A.; Luna, C. A. M.; Köhler, J.; Bisquert, J.; Hildner, R.; Huettner, S. Real-time observation of iodide ion migration in methylammonium lead halide perovskites. *Small* **2017**, *13*, 1701711.
(37) Amerling, E.; Baniya, S.; Lafalce, E.; Zhang, C.; Vardeny, Z. V.; Whittaker-Brooks, L. Electroabsorption spectroscopy studies of $(C_4H_9NH_3)_2PbI_4$ organic−inorganic hybrid perovskite multiple quantum wells. *J. Phys. Chem. Lett.* **2017**, *8*, 4557−4564.
(38) Ziffer, M. E.; Mohammed, J. C.; Ginger, D. S. Electroabsorption spectroscopy measurements of the exciton binding energy, electron−hole reduced effective mass, and band gap in the perovskite $CH_3NH_3PbI_3$. *ACS Photonics* **2016**, *3*, 1060−1068.
(39) Zhai, Y.; Baniya, S.; Zhang, C.; Li, J.; Haney, P.; Sheng, C.-X.; Ehrenfreund, E.; Vardeny, Z. V. Giant Rashba splitting in 2D organic-inorganic halide perovskites measured by transient spectroscopies. *Sci. Adv.* **2017**, *3*, No. e1700704.
(40) Wu, X.; Yu, H.; Li, L.; Wang, F.; Xu, H.; Zhao, N. Composition-dependent light-induced dipole moment change in organometal halide perovskites. *J. Phys. Chem. C* **2015**, *119*, 1253−1259.
(41) Li, C.; Tscheuschner, S.; Paulus, F.; Hopkinson, P. E.; Kießling, J.; Köhler, A.; Vaynzof, Y.; Huettner, S. Iodine migration and its effect on hysteresis in perovskite solar cells. *Adv. Mater.* **2016**, *28*, 2446−2454.
(42) Kahle, F.-J.; Saller, C.; Olthof, S.; Li, C.; Lebert, J.; Weiß, S.; Herzig, E. M.; Hüttner, S.; Meerholz, K.; Strohriegl, P.; et al. Does eectron delocalization influence charge separation at donor−acceptor interfaces in organic photovoltaic cells? *J. Phys. Chem. C* **2018**, *122*, 21792−21802.
(43) Li, C.; Vaynzof, Y.; Lakhwani, G.; Beirne, G. J.; Wang, J.; Greenham, N. C. Observation of oxygen vacancy migration in memory devices based on ZnO nanoparticles. *J. Appl. Phys.* **2017**, *121*, 144503.
(44) Campbell, I. H.; Hagler, T. W.; Smith, D. I.; Ferraris, J. P. Direct measurement of conjugated polymer electronic excitation energies using metal/polymer/metal structures. *Phys. Rev. Lett.* **1996**, *76*, 1900.
(45) Bisquert, J. *Nanostructured energy devices: Equilibrium concepts and kinetics*; CRC Press, 2014.
(46) Nian, Y. B.; Strozier, J.; Wu, N. J.; Chen, X.; Ignatiev, A. Evidence for an oxygen diffusion model for the electric pulse induced resistance change effect in transition-metal oxides. *Phys. Rev. Lett.* **2007**, *98*, 146403.
(47) Manthiram, A.; Yu, X.; Wang, S. Lithium battery chemistries enabled by solid-state electrolytes. *Nat. Rev. Mater.* **2017**, *2*, 16103.
(48) Sun, C.; Liu, J.; Gong, Y.; Wilkinson, D. P.; Zhang, J. Recent advances in all-solid-state rechargeable lithium batteries. *Nano Energy* **2017**, *33*, 363−386.
(49) Yu, H.; Wang, F.; Xie, F.; Li, W.; Chen, J.; Zhao, N. The role of chlorine in the formation process of "$CH_3NH_3PbI_{3-x}Cl_x$" perovskite. *Adv. Funct. Mater.* **2014**, *24*, 7102−7108.
(50) Li, C.; Guerrero, A.; Huettner, S.; Bisquert, J. Unravelling the role of vacancies in lead halide perovskite through electrical switching of photoluminescence. *Nat. Commun.* **2018**, *9*, 5113.
(51) Xing, J.; Wang, Q.; Dong, Q.; Yuan, Y.; Fang, Y.; Huang, J. Ultrafast ion migration in hybrid perovskite polycrystalline thin films under light and suppression in single crystals. *Phys. Chem. Chem. Phys.* **2016**, *18*, 30484−30490.
(52) Lee, D. S.; Yun, J. S.; Kim, J.; Soufiani, A. M.; Chen, S.; Cho, Y.; Deng, X.; Seidel, J.; Lim, S.; Huang, S.; et al. Passivation of grain boundaries by phenethylammonium in formamidinium-methylammonium lead halide perovskite solar cells. *ACS Energy Lett.* **2018**, *3*, 647−654.
(53) Chen, S.; Wen, X.; Sheng, R.; Huang, S.; Deng, X.; Green, M. A.; Ho-Baillie, A. Mobile ion induced slow carrier dynamics in organic−inorganic perovskite $CH_3NH_3PbBr_3$. *ACS Appl. Mater. Interfaces* **2016**, *8*, 5351−5357.
(54) Zhao, Y.; Zhou, W.; Ma, W.; Meng, S.; Li, H.; Wei, J.; Fu, R.; Liu, K.; Yu, D.; Zhao, Q. Correlations between immobilizing ions and suppressing hysteresis in perovskite solar cells. *ACS Energy Lett.* **2016**, *1*, 266−272.

DOI: 10.1021/acs.jpclett.9b02467
J. Phys. Chem. Lett. 2019, 10, 6857−6864